# Dynamic model of the radio-frequency plasma sheath in a highly asymmetric discharge cell

M. A. Sobolewski
*National Institute of Standards and Technology, Gaithersburg, Maryland 20899*
(Received 11 December 1996; revised manuscript received 28 March 1997)

A self-consistent fluid model for the radio-frequency sheath at the powered electrode of a highly asymmetric discharge cell is developed and solved. The model assumes time-independent ion motion and inertialess electrons. The voltage on the powered electrode, assumed to be sinusoidal, is shared between the powered sheath and a series resistance that represents the remainder of the discharge. The model includes ion collisions, sheath conduction currents, and secondary electron emission from the electrode surface. Model results are compared with previous sheath models and with experiment. Current wave forms predicted by the model closely resemble the nonsinusoidal current wave forms measured in highly asymmetric cells. The model accurately predicts the shape of sheath voltage wave forms, but not their dc components. The magnitudes and phases of sheath impedances predicted by the model agree with experimental measurements performed in argon discharges at pressures of 4.0–133 Pa. [S1063-651X(97)07007-4]

PACS number(s): 52.65.−y, 52.80.Pi, 52.40.−w

## I. INTRODUCTION

When radio-frequency (rf) current flows between an electrode and a plasma, rf voltage is developed across the intervening space-charge sheath. The resulting rf sheath has important electrical properties that are not yet fully understood. Usually, rf sheaths make dominant contributions to the electrical characteristics of rf discharges. Thus a better understanding of sheath properties could aid in the design of rf discharge cells and the circuitry that powers them. It could also result in improved methods of monitoring and controlling rf discharges.

A rf sheath is a nonlinear device—its electrical properties depend on the rf amplitude and on the properties of the electrical network that surrounds it. Sheath properties also vary with pressure and frequency. At frequencies much higher than the ion plasma frequency, the sheath is primarily capacitive. Self-consistent fluid models of capacitive rf sheaths have been derived by Lieberman [1,2], using a formalism that consists of a stationary ion profile and an oscillating, steplike electron profile. One model [1] covers the low-pressure regime, where ion collisions can be neglected; the other [2] covers the high-pressure, highly collisional regime. Godyak and Sternberg [3] have extended the oscillating-step formalism to cover the entire pressure range. Their model also includes the flow of conduction current across the sheath; the Lieberman models only consider displacement current. All three models assume that the current flowing through the sheath is sinusoidal, a reasonable assumption for symmetric discharges. Most plasma reactors, however, have a grounded area larger than the powered electrode area. In these asymmetric reactors, voltage wave forms are much more sinusoidal than current wave forms. Sheaths excited by sinusoidal voltages have been modeled [4–6], but only under rather limiting restrictions. Some models are not self-consistent; they rely on arbitrary assumptions about the nonlinear sheath capacitance [4] or the ion profile in the sheath [5]. One kinetic model of the rf sheath [6] has been solved self-consistently, but that work neglected ion collisions, so it applies only at very low pressures.

This paper presents a sheath model designed for asymmetric discharges at high frequencies, in the pressure range where ion collisions are important. In particular, we simulate the sheath at the powered electrode of the highly asymmetric reactor of Refs. [7,8] for argon plasmas at 4.0–133 Pa. The model is based on the same oscillating-step formalism of Refs. [1–3]. Here, however, the applied voltage is assumed to be sinusoidal, not the current. The applied voltage is shared between the sheath and a series resistance which represents the impedance of the remainder of the discharge, observed to be primarily resistive [7]. The model includes the flow of conduction current across the sheath. Emission of secondary electrons from the electrode is also included.

First, the model will be described, including its assumptions, the method of solution, and the range of input parameters investigated here. Then model predictions for the current and voltage wave forms, the fundamental magnitude and phase of the sheath impedance, and the dc component of sheath voltage will each be discussed and compared with previous models and with experiment. A final section summarizes the results, and identifies issues that deserve further study.

## II. MODEL OF THE SHEATH

A sketch of the sheath model is given in Fig. 1. The model is one-dimensional—edge effects and lateral nonuniformities are ignored—so position in the sheath is indicated by a single spatial coordinate $x$, increasing from the plasma towards the electrode. The sheath contains electrons and a single species of positive ions. The ion density profile $n_i(x)$ is assumed to be independent of time $t$ but the electron density profile $n_e(x,t)$ is not. Instead, $n_e(x,t)$ consists of a sharp, steplike drop in electron density that lies at a time-varying position called the instantaneous sheath edge. The distance between the instantaneous sheath edge and the electrode is the instantaneous sheath width $W(t)$. During each rf cycle $W(t)$ oscillates between a minimum value $W_{\min}$ in the vicinity of the electrode, and a maximum value $W_{\max}$. The point of maximum expansion, $W(t)=W_{\max}$, defines the in-

 

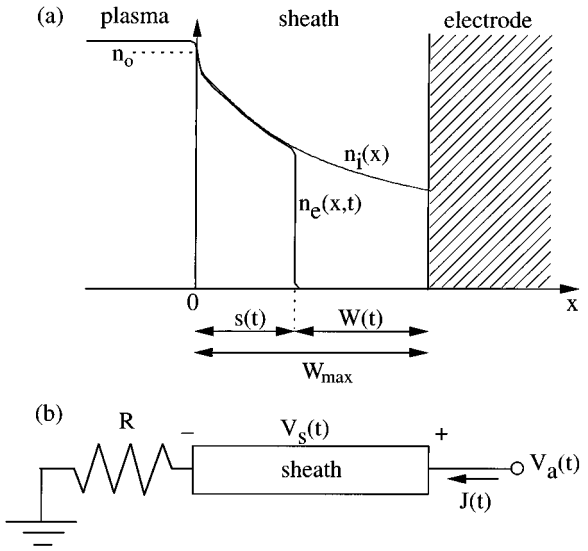


FIG. 1. The sheath model. (a) Cross section through the sheath showing the time-independent ion density profile $n_i(x)$ and the time-dependent electron density profile $n_e(x,t)$. The sheath-presheath boundary is at $x=0$, the surface of the electrode is at $x=W_{\max}$, and the steplike drop in $n_e(x)$ occurs at a distance $s(t)$ from the former, $W(t)$ from the latter. (b) Definition of $J(t)$ and $V_s(t)$, the sheath current and voltage wave forms, and the electrical circuit surrounding the sheath. The voltage on the powered electrode, $V_a(t)$, is shared between the sheath and a series resistance $R$.

terface between the sheath and the presheath. (The presheath region between the sheath and the unperturbed plasma is considered part of the plasma, not the sheath.) The sheath-presheath interface serves as the origin of the $x$ axis. The position of the instantaneous sheath edge relative to the origin is $s(t)$, where $s(t)=W_{\max}-W(t)$.

On the plasma side of the instantaneous sheath edge, the quasineutrality condition $n_e=n_i$ is assumed; on the other side, it is assumed that $n_e=0$. Therefore

$$n_e(x)=\begin{cases} n_i(x), & x<s(t) \\ 0, & x\geqslant s(t). \end{cases} \tag{1}$$

The electron charge is $-q$, and the ion charge is assumed to be $+q$, so the charge density $\rho(x,t)$ is given by $\rho(x,t)=q(n_i-n_e)$. The electric field $E(x,t)$ and the electrostatic potential $V(x,t)$ are therefore determined from Gauss's law and Poisson's equation as

$$-\frac{\partial^2 V}{\partial x^2}=\frac{\partial E}{\partial x}=\frac{\rho}{\varepsilon_0}=\begin{cases} 0, & x<s(t) \\ qn_i(x)/\varepsilon_0, & x\geqslant s(t). \end{cases} \tag{2}$$

The total voltage drop across the sheath, $V_s(t)$, is

$$V_s(t)=V(W_{\max},t)-V(0,t). \tag{3}$$

Thus $\rho(x,t)$ and $E(x,t)$ are always $\geqslant 0$, while $V(x,t)$ and $V_s(t)$ are always $\leqslant 0$.

Ion dynamics are modeled by a fluid representation, in which the mean ion drift velocity directed towards the electrode, $u_i(x)$, is governed by the ion momentum conservation equation [3]

$$u_i\partial u_i/\partial x+\pi u_i^2/2\lambda_i=q\langle E\rangle/m_i, \tag{4}$$

where $m_i$ is the ion mass and $\lambda_i$ is the ion diffusivity mean free path, assumed to be independent of $u_i$. The first term is the ion acceleration, the second arises from the ion drag force, and the third arises from the electric force. The ions are assumed to be too massive to respond to the rf components of the electric field, so no rf field components (and no time derivatives) appear in Eq. (4). Only the time-averaged electric field $\langle E\rangle$ appears. The ion diffusion term has also been neglected, because the ion drift velocity everywhere is assumed to be much greater than the ion thermal velocity.

The ion density $n_i$ and velocity $u_i$ are related by the ion conservation equation. If $n_i$ does not depend on time, and if ions are neither created nor destroyed in the sheath, then

$$\partial(n_iu_i)/\partial x=0. \tag{5}$$

Therefore the ion current $J_i$ is constant in space as well as time.

$$J_i=-qn_iu_iA=-qn_0u_0A, \tag{6}$$

where $n_0$ and $u_0$ are the ion density and velocity at $x=0$, and $A$ is the area of the electrode. Because the electric field accelerates the ions towards the electrode, $u_i$ increases with $x$, and $n_i$ must therefore decrease with $x$, as in Fig. 1.

In contrast, electrons are repelled by the electric field. To reach the electrode, they must be thermally excited over a barrier of height $qV(s,t)-qV(W_{\max},t)$, presented by the voltage difference between the electrode and the instantaneous sheath edge. Assuming that the electrons have a Maxwell-Boltzmann velocity distribution, always in equilibrium with the rf potential, with time-independent temperature $T_e$, the electron current is

$$J_e=qAn_i(s)\left(\frac{qT_e}{2\pi m_e}\right)^{1/2}\exp\left(\frac{-V(s,t)+V(W_{\max},t)}{T_e}\right), \tag{7}$$

where $m_e$ is the electron mass, $T_e$ is in units of voltage, and Eq. (1) has been used to set $n_e(s)=n_i(s)$. There is also a current of secondary electrons, $J_s=Y_iJ_i-Y_eJ_e$, where $Y_i$ is the yield of secondary electrons per incident ion (assumed to be independent of ion energy), and $Y_e$ is the yield per incident primary electron (also energy independent). The secondary electrons, like the primary electrons, are assumed to have negligible inertia, so no modification of Eq. (1) is needed to account for them. Ionization produced by secondary electrons within the sheath is not included in the model.

The sum of electron and ion currents is the conduction current

$$J_c=(1+Y_i)J_i+(1-Y_e)J_e. \tag{8}$$

In addition to the conduction current, there is a displacement current [3]

$$J_d=-\varepsilon_0AdE(W_{\max},t)/dt=qn_i(s)Ads/dt. \tag{9}$$

The total current $J$ is the sum of $J_c$ and $J_d$,

$$J=J_c+J_d. \tag{10}$$

To solve Eqs. (1)–(10) one must specify $n_0$, $u_0$, and $E_0$, the ion density, ion velocity, and electric field at the sheath-presheath interface, which are all assumed to be independent of time. One must also specify additional equations to describe the electrical circuit that surrounds the sheath, here assumed to be the sheath at the powered electrode of a highly asymmetric reactor. First, the time-averaged current through the sheath is zero,

$$\langle J(t)\rangle = \langle (1+Y_i)J_i + (1-Y_e)J_e\rangle = 0. \tag{11}$$

One need not include the displacement current because its time average is identically zero. Second, the voltage on the powered electrode, $V_a(t)$, is assumed to be sinusoidal,

$$V_a(t) = V_{a0} + V_{a1}\cos(\omega t + \delta), \tag{12}$$

where $\omega$ is the (angular) frequency. Third, the applied voltage $V_a(t)$ is the sum of the voltage across the sheath, $V_s(t)$, and the voltage $V_r(t)$ across the remainder of the discharge,

$$V_a(t) = V_s(t) + V_r(t), \tag{13}$$

where $V_r(t)$ is defined by

$$V_r(t) = RJ(t). \tag{14}$$

$R$ represents the resistance of the bulk plasma and the sheaths at all grounded surfaces. It also includes $R_e$, the resistance associated with the boundary between the plasma and the powered electrode sheath [7]. For simplicity, the model neglects any reactance contributed by the cell, the ground sheaths, or the plasma. The nonlinearity of the sheaths at the grounded surfaces is also neglected.

To compare the model with experiment, it should be noted that the model wave forms $J(t)$ and $V_a(t)$ defined here are equivalent to the wave forms $I_{\rm pe}(t)$ and $V_{\rm pe}(t)$ used in experimental studies [7,8]. The model sheath voltage wave form $V_s(t)$ is related to the measured ''sheath voltage'' wave form $V_{\rm ps}(t)$ by

$$V_s(t) = V_{\rm ps}(t) - I_{\rm pe}(t)R_e, \tag{15}$$

where the resistance $R_e$ is determined experimentally using fitting procedures [7,9].

### A. Input parameters

It is convenient to express the input parameters in normalized, i.e., dimensionless, form. This is accomplished by dividing all particle and charge densities by $n_0$, dividing all voltages by $T_e$, dividing the ion velocity $u_i$ by the Bohm velocity

$$u_B = (qT_e/m_i)^{1/2}, \tag{16}$$

dividing frequencies (and multiplying times) by the frequency $\omega$, dividing the distances $x$, $s$, $W$, and $\lambda_i$ by the Debye length

$$\lambda_D = (\varepsilon_0 T_e/qn_0)^{1/2}, \tag{17}$$

dividing the electric field by $T_e/\lambda_D$, dividing impedances by

$$Z_D = \lambda_D/\omega\varepsilon_0 A, \tag{18}$$

and dividing currents by

$$J_D = T_e/Z_D = qn_0\omega\lambda_D A. \tag{19}$$

$Z_D$ is the capacitive impedance of parallel plates of the same area as the electrode, separated by one Debye length. $J_D$ is the current that such a capacitor would draw if a rf voltage of amplitude $T_e$ were applied across it.

To obtain a solution, one must specify the following dimensionless parameters: a collisional parameter $\lambda_i/\lambda_D$; the sheath width $W_{\rm max}/\lambda_D$; the dimensionless boundary conditions for ion injection velocity, electric field, and series resistance, $u_0/u_B$, $E_0\lambda_D/T_e$, and $R/Z_D$; the secondary electron yields $Y_i$ and $Y_e$, and two additional parameters $\omega_i/\omega$ and $\omega_e/\omega$, where $\omega_i$ and $\omega_e$ are the ion and electron plasma frequencies,

$$\omega_i = (q^2 n_0/m_i\varepsilon_0)^{1/2} = u_B/\lambda_D, \tag{20}$$

$$\omega_e = (q^2 n_0/m_e\varepsilon_0)^{1/2} = (m_i/m_e)^{1/2}\omega_i. \tag{21}$$

Factors of $\omega_i/\omega$ and $\omega_e/\omega$ appear in the equations for the ion and electron currents, Eqs. (6) and (7), when they are normalized.

$$J_i/J_D = (u_0/u_B)(\omega_i/\omega), \tag{22}$$

$$\frac{J_e}{J_D} = -\frac{1}{\sqrt{2\pi}}\frac{n_i(s)}{n_0}\frac{\omega_e}{\omega}\exp\left(\frac{-V(s,t)+V(W_{\rm max},t)}{T_e}\right). \tag{23}$$

Values of the input parameters were chosen to simulate the experimental conditions of a previous study [8] of argon discharges at pressures of 4.0–133 Pa (0.03–1.0 Torr) in the Gaseous Electronics Conference (GEC) rf Reference Cell. Table I lists values of the experimental parameters. Table II lists values for the corresponding dimensionless parameters. As noted previously [3], the assumptions made above that the electrons have negligible inertia and that $n_0$, $u_0$, $E_0$, $n_i(x)$, and $u_i(x)$ are time independent are valid in the limits $(\omega_i/\omega)^2 \ll 1$ and $(\omega_e/\omega)^2 \gg 1$. The values of $\omega_i/\omega$ and $\omega_e/\omega$ given in Table II show that these criteria are nearly or completely satisfied over the entire experimental range. Values of $V_{s1}/T_e$ are given in Table II, but $V_{s1}/T_e$ is not actually an input parameter. Instead, the input parameter $W_{\rm max}/\lambda_D$ was varied until solutions for the desired values of $V_{s1}/T_e$ were obtained. The parameters $Y_i$, $Y_e$, $u_0/u_B$, and $E_0\lambda_D/T_e$ are not listed in Table II. Most results reported here were obtained at $Y_i = Y_e = 0$, but these results differ by less than 2% from results obtained using values of $Y_i \approx 0.1$ and $Y_e \approx 0.2$, measured on aluminum electrodes at low incident energies [10–12]. Values for $u_0/u_B$ and $E_0\lambda_D/T_e$ were not determined by experiment; rather, they were obtained from the Godyak-Sternberg theory of the presheath [3,13], described in the next section.

### B. Model of the presheath

In models of collisionless, dc plasma sheaths, the requirement that the ion density profile fall off less rapidly with distance than the electron density profile (a necessary condition for the formation of a sheath with a net positive charge) imposes a lower bound on allowed values of $u_0$, the ion

TABLE I. Experimental conditions for argon discharges in the GEC rf Reference Cell, at $\omega/2\pi=13.56$ MHz, at pressures of 4–133 Pa. The amplitude of the fundamental component of the voltage across the sheath at the powered electrode, $V_{s1}$, the total resistance in series with the powered sheath, $R$, and the ion current at the powered electrode, $J_i$, were measured in Ref. [8], for many voltages. Only the highest and lowest voltage at each pressure are shown. The electron temperature $T_e$ was obtained from Langmuir probe measurements in this cell and in other GEC cells [19,20]. Values of the mean free path of $Ar^+$, the dominant ion in these discharges [21], was calculated [8] from measurements [22] of the cross section of Ar symmetric charge exchange collisions. From $J_i$, $T_e$, and $\lambda_i$, estimates for $n_0$, the electron density at the boundary between the plasma and the powered sheath, were obtained using Eqs. (6), (16), (17), and (27).

| Pressure (Pa) | $V_{s1}$ (V) | $R$ (Ω) | $J_i$ (mA) | $T_e$ (eV) | $\lambda_i$ (mm) | $n_0$ ($10^8$ cm$^{-3}$) |
|---|---|---|---|---|---|---|
| 4.0 | 34 | 282 | 0.57 | 3 | 2.2 | 2.1 |
| 13.3 | 27 | 224 | 0.63 | 3 | 0.66 | 3.0 |
| 40.0 | 25 | 173 | 0.90 | 3 | 0.22 | 5.7 |
| 133.3 | 24 | 140 | 1.33 | 3 | 0.066 | 12.2 |
| 4.0 | 401 | 30 | 9.4 | 3 | 2.2 | 29 |
| 13.3 | 356 | 22 | 14.3 | 3 | 0.66 | 49 |
| 40.0 | 324 | 17 | 22.8 | 3 | 0.22 | 92 |
| 133.3 | 176 | 22 | 24.2 | 3 | 0.066 | 133 |

injection velocity [14]. The limiting velocity is the Bohm velocity $u_B$ of Eq. (16). In rf sheaths, however, the rf modulation of the sheath width causes the time-averaged electron density to fall off more slowly than in dc sheaths, so solutions can be obtained even at $u_0<u_B$. Indeed, in oscillating-step models, the ion density always falls off more slowly than the time-averaged electron density and solutions may be obtained at arbitrarily low $u_0/u_B$. On the other hand, there is an upper bound on ion injection velocity. The equation

$$\frac{\lambda_D}{n_0}\frac{dn_i}{dx}\bigg|_{x=0}=-\frac{E_0\lambda_D}{T_e}\left(\frac{u_0}{u_B}\right)^{-2}+\frac{\pi\lambda_D}{2\lambda_i}, \tag{24}$$

obtained from Eqs. (4), (5), and (16), demonstrates that, if $u_0/u_B$ is too large, the initial slope of the $n_i(x)$ profile will be positive. This indicates that ions are initially decelerated when they enter the sheath. A deceleration of the ions might be possible, if ions drifted from a region of no collisions into a region of frequent collisions. But deceleration of ions is not reasonable or likely in the rf plasma sheath. If collisions occur in the sheath, they should occur in the presheath as well.

If the initial slope of the ion profile is to have the correct (negative) sign, the ion velocity is restricted by Eq. (24) to the range

$$(u_0/u_B)^2<(E_0\lambda_D/T_e)(2\lambda_i/\pi\lambda_D). \tag{25}$$

Any theory of the presheath that includes collisions should predict values of $E_0\lambda_D/T_e$ and $u_0/u_B$ that satisfy this condition. The Godyak-Sternberg model of the presheath [3,13], used here, predicts

$$E_0\lambda_D/T_e=1, \tag{26}$$

TABLE II. Estimates of the values of the model parameters that correspond to the experimental conditions of Table I. The values were calculated from Table I, Eqs. (16)–(21), and an ion mass $m_i$ corresponding to $Ar^+$.

| Pressure (Pa) | $V_{s1}/T_e$ | $\lambda_i/\lambda_D$ | $u_0/u_B$ | $\omega_i/\omega$ | $\omega_e/\omega$ | $R/Z_D$ |
|---|---|---|---|---|---|---|
| 4.0 | 11.3 | 2.46 | 0.78 | 0.036 | 9.6 | 1.94 |
| 13.3 | 8.9 | 0.89 | 0.60 | 0.043 | 11.5 | 1.85 |
| 40.0 | 8.3 | 0.41 | 0.45 | 0.059 | 15.9 | 1.96 |
| 133.3 | 8.0 | 0.18 | 0.32 | 0.086 | 23.2 | 2.31 |
| 4.0 | 134 | 9.18 | 0.92 | 0.133 | 35.8 | 0.76 |
| 13.3 | 119 | 3.58 | 0.83 | 0.173 | 46.6 | 0.72 |
| 40.0 | 108 | 1.63 | 0.71 | 0.236 | 63.6 | 0.79 |
| 133.3 | 59 | 0.59 | 0.52 | 0.284 | 76.6 | 1.22 |

$$u_0/u_B=[1+\pi\lambda_D/(2\lambda_i)]^{-1/2}, \tag{27}$$

which always satisfy Eq. (25).

### C. Method of solution

Solutions are obtained by an iterative, numerical process. First, an initial guess for $n_i(x)/n_0$, the ion profile, is assumed, and Eqs. (1)–(3) and (6)–(14) are solved to determine the electric field $E(x,t)\lambda_D/T_e$ at every point in space and time. The field is then averaged over time, and the time average is inserted into Eqs. (4) and (5) to calculate a new, more accurate ion profile. This process iterates until $n_i(x)/n_0$ converges.

The solution of Eqs. (1)–(3) and (6)–(14) is itself an iterative process. Initially, the current $J(t)/J_D$, the sheath width $W(t)/\lambda_D$, the sheath voltage $V_s(t)/T_e$, and the applied voltage $V_a(t)/T_e$, are known only at $t_{\max}$, the time when the sheath reaches its maximum expansion. The known value $V_a(t_{\max})/T_e$ and assumed values for $V_{a0}/T_e$ and $V_{a1}/T_e$ completely determine the applied voltage wave form in Eq. (12) at all times. Then, at every time point, an iterative procedure determines $W(t)/\lambda_D$ and all other wave forms. This procedure is repeated for varying values of $V_{a0}/T_e$ and $V_{a1}/T_e$, until $W(t)/\lambda_D$ has the correct rf periodicity, and the requirement of no net current, Eq. (11), is satisfied.

## III. WAVE FORMS

Examples of calculated wave forms are shown in Fig. 2. First, in Fig. 2(a), the position of the instantaneous sheath edge is plotted. Two vertical scales are provided, both normalized by the Debye length. One, $W(t)$, is the position of the sheath edge referenced to the electrode; the other, $s(t)$, is referenced to the sheath-presheath boundary. The horizontal axis is time in radians, with the start of the cycle, at $\omega t=-\pi$, defined as the time of maximum expansion of the sheath, $t_{\max}$. Starting at $t_{\max}$, the sheath contracts and the sheath width $W(t)$ falls from its initial value $W_{\max}=25\lambda_D$, reaching a minimum value $W_{\min}=0.95\lambda_D$ at time $t_{\min}$, slightly more than half a cycle later. Then, for the remainder of the cycle, the sheath expands.

Figure 2(b) shows the conduction current and displace-

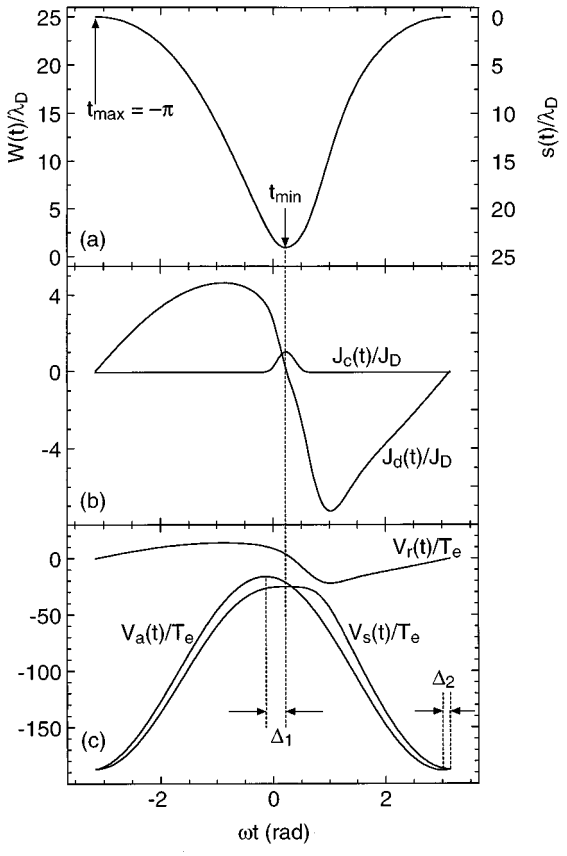


FIG. 2. Calculated wave forms, in dimensionless units, for (a) the position $W(t)$ of the instantaneous sheath edge relative to the electrode and its position $s(t)$ relative to the plasma-sheath boundary, (b) the conduction and displacement currents, $J_c(t)$ and $J_d(t)$, and (c) the sheath voltage $V_s(t)$, the voltage $V_r(t)$ across the series resistor $R$, and their sum, the applied voltage $V_a(t)$. The wave forms were calculated for $W_{\max}/\lambda_D=25$, $u_0/u_B=0.62$, $\lambda_i/\lambda_D=1.0$, $E_0\lambda_D/T_e=1.0$, $R/Z_D=3.0$, $\omega_i/\omega=0.10$, $\omega_e/\omega=27.0$, and $Y_i=Y_e=0$.

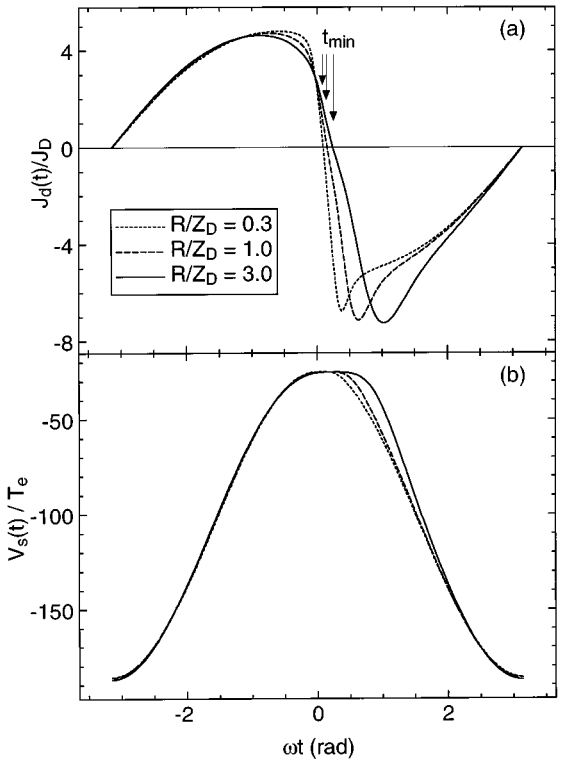


FIG. 3. Wave forms for (a) the displacement current and (b) the sheath voltage, calculated at three different values of $R/Z_D$. Values of the other input parameters are given in Fig. 2.

ment current, $J_c(t)$ and $J_d(t)$. As expected from Eqs. (6)–(8), $J_c(t)$ consists of a positive peak of electron current centered at time $t_{\min}$, when the barrier to electron flow is lowest, and a constant ion current $-0.062J_D$, so small it is difficult to see. Roughly, $J_d(t)$ varies as $ds/dt$, but Eq. (9) shows that they are not strictly proportional, because of the time-varying factor $n_i(s)$. The total current $J(t)$ is not shown. During most of the cycle, $J_d(t)$ dominates $J_c(t)$, so $J(t)\approx J_d(t)$.

Figure 2(c) shows the sinusoidal applied voltage $V_a(t)$, the sheath voltage $V_s(t)$, and the voltage $V_r(t)$ dropped across the series resistance. According to Eq. (14), $V_r(t)$ is proportional to $J(t)$. $J(t)$ is not sinusoidal, so $V_r(t)$ is not, and, because of Eq. (13), neither is $V_s(t)$. In the region near $t_{\min}$, where the conduction current is significant, $V_s(t)$ is flat. This flattening is analogous to the clipping produced by a resistor and a diode in series. The sheath plays the role of the diode, because the electron conduction current has an exponential dependence on voltage. Figure 3 shows that this clipping becomes more visible as $R/Z_D$ increases. As $R/Z_D$ decreases, $V_s(t)$ becomes more sinusoidal.

The extrema of $V_s(t)$ occur at $t_{\max}$ and $t_{\min}$ but the extrema of $V_a(t)$ do not. At $t_{\max}$ and $t_{\min}$, $dW/dt=0$, $dV_s/dt=0$, $dJ_c/dt=0$, and, from Eq. (13),

$$dV_a/dt=dV_s/dt+RdJ/dt=RdJ_d/dt\neq 0. \qquad (28)$$

Thus $dV_a/dt$ has the same sign as $dJ_d/dt$, negative at $t_{\min}$, positive at $t_{\max}$. Therefore the maximum (and minimum) of $V_a(t)$ must occur slightly before the maximum (and minimum) of $V_s(t)$. The magnitude of $dJ_d/dt$ is larger at $t_{\min}$ that at $t_{\max}$, so the offset in the maxima of $V_a$ and $V_s$, labeled $\Delta_1$ in Fig. 2(c), is larger than the offset in their minima, labeled $\Delta_2$. Because $\Delta_1>\Delta_2$, the sheath spends more than half of the cycle contracting and less than half of the cycle expanding. As $R\rightarrow 0$, Eq. (28) forces $\Delta_1$ and $\Delta_2$ to zero, and the fraction of the rf period during which the sheath contracts approaches one-half. This can be seen in Fig. 3; as $R/Z_D$ decreases, the time $t_{\min}$ shifts to the left, approaching zero. Thus it is the interaction of $R$ and $J_d(t)$ that makes the contraction last longer than the expansion. In contrast, when $R$ is replaced by a series capacitor $C$ so that $J=CdV_r/dt$, the extrema of $V_a(t)$ occur after the extrema of $V_s(t)$, the sheath instead spends more of the cycle expanding than contracting, and no clipping is observed.

Wave forms predicted by the model are in good agreement with experiment. For example, an experimental current wave form from Ref. [7] shown in Fig. 4, has a shape that is quite similar to the corresponding model wave form. The measured wave form does not have the sinusoidal form assumed by models of symmetric discharges [1–3], nor does it resemble the nonsinusoidal current wave forms predicted by a previous model of asymmetric discharges [5]. That model, which assumes a sinusoidal sheath voltage and neglects the

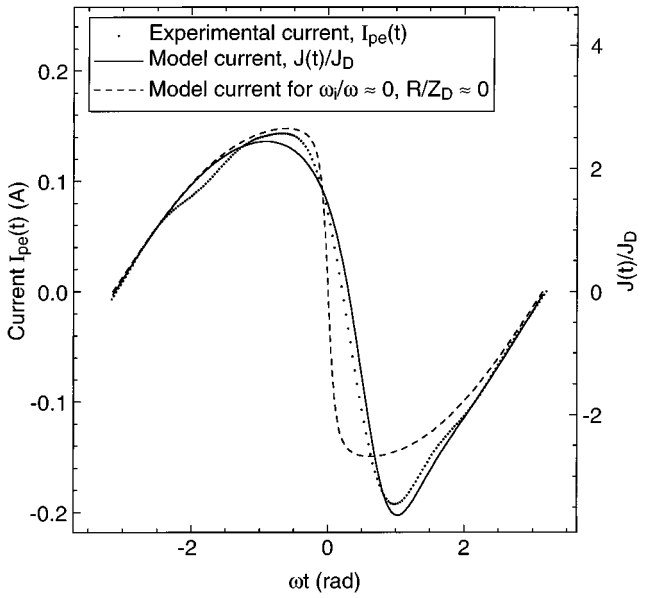


FIG. 4. Comparison of theoretical and experimental current wave forms. The experimental wave form $I_{pe}(t)$ was measured at 13.3 Pa, $V_{ps1}=67$ V, $R_e=36\,\Omega$, and $R=69\,\Omega$. Input parameters for the complete model (solid curve) were $W_{max}/\lambda_D=12.2$, $\lambda_i/\lambda_D=1.45$, $u_0/u_B=0.69$, $\omega_i/\omega=0.070$, $\omega_e/\omega=18.9$, $R/Z_D=1.36$, $E_0\lambda_D/T_e=1.0$, and $Y_i=Y_e=0$. Model results are also shown for another case (dashed line), with $\omega_i/\omega=0.001$, $\omega_e/\omega=0.27$, $R/Z_D=0.001$, and the other parameters unchanged, which illustrates the shape of the wave forms calculated in Ref. [5].

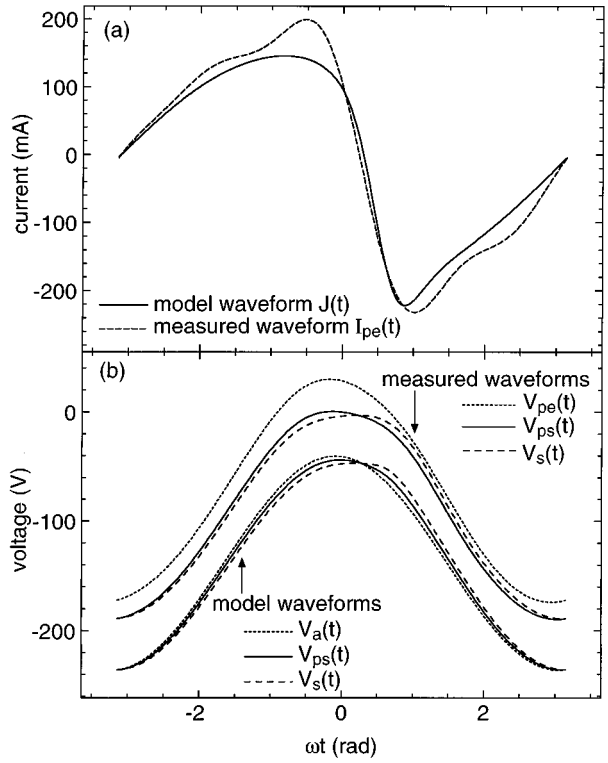


FIG. 5. Comparison of theoretical and experimental wave forms of (a) current and (b) voltage. The experimental voltage wave forms are the voltage on the powered electrode, $V_{pe}(t)$, the voltage $V_{ps}(t)$ across the powered sheath, and the voltage $V_s(t)$ obtained from the measured $V_{ps}(t)$ using Eq. (15). The theoretical voltage wave forms are the applied voltage $V_a(t)$, the sheath voltage $V_s(t)$, and the voltage $V_{ps}(t)$ calculated from the model $V_s(t)$ using Eq. (15). The experimental conditions were 13.3 Pa, $V_{ps1}=98$ V, $J_i=3.2$ mA, $R_e=36\,\Omega$, $R=69\,\Omega$. Model parameters were $W_{max}/\lambda_D=15.5$, $V_{s1}/T_e=32.2$, $\lambda_i/\lambda_D=1.82$, $u_0/u_B=0.73$, $\omega_i/\omega=0.088$, $\omega_e/\omega=23.6$, $R/Z_D=1.17$, $E_0\lambda_D/T_e=1.0$, and $Y_i=Y_e=0$.

sheath conduction current, can be reproduced by solving the more general model presented here in the limits $R/Z_D \ll 1$, and $\omega_i/\omega \ll 1$. The current wave form obtained from one such solution, shown in the figure, does not fit the data.

In Fig. 5, model results are compared to wave forms measured (but not reported) in Ref. [8]. The ion current measurements performed in that study provide enough information to allow absolute comparisons between the model and experiment (at the cost of a slight reduction in the bandwidth of the electrical measurements relative to Ref. [7]). Current wave forms are compared in Fig. 5(a). The measured current wave form has a larger amplitude than the model wave form. Consequently, the measured sheath impedance is smaller than the model predicts, as will be discussed in Sec. V, below.

Model voltage wave forms are compared with experiment in Fig. 5(b). The shapes of the model wave forms agree reasonably well with experiment. The experimental $V_{ps}(t)$ and $V_s(t)$ wave forms are clipped and skewed, as predicted by the model. Although the model assumes that the applied voltage wave form $V_a(t)$ is a perfect sinusoid, the analogous experimental wave form $V_{pe}(t)$ is not. Repeating the model calculations using measured, nonsinusoidal $V_{pe}(t)$ wave forms might increase the accuracy of the model predictions, but such calculations are beyond the scope of this paper. The rf and dc amplitudes of $V_a(t)$ differ from $V_{pe}(t)$ because the capacitance and rectification contributed by the sheath at grounded cell surfaces are not included in the model. The dc offset between the predicted and measured $V_{ps}(t)$ [and $V_s(t)$] wave forms will be discussed below, in Sec. VI.

## IV. IMPEDANCE PHASE

The magnitude and phase of the fundamental components of the calculated wave forms, $J(t)$, $J_c(t)$, $J_d(t)$, $V_s(t)$, and $V_a(t)$ are represented by the complex Fourier coefficients, $J_1$, $J_{c1}$, $J_{d1}$, $V_{s1}$, and $V_{a1}$. Together, $J_1$ and $V_{a1}$ define the total impedance,

$$Z_a = V_{a1}/J_1, \tag{29}$$

which is equivalent to the impedance $Z_{pe}$ defined in experimental studies [7,8]. Also, $J_1$ and $V_{s1}$ define an impedance

$$Z_s = V_{s1}/J_1, \tag{30}$$

which is the impedance of the sheath itself, excluding the resistance $R$. In experiments [7,8], $Z_s$ is determined from the measured impedance $Z_{ps}$, using

$$Z_s = Z_{ps} - R_e, \tag{31}$$

from Eqs. (15) and (30). In addition to $Z_s$, experimental studies make use of $C_s$, the sheath capacitance, and $Z_c$, the capacitive part of the sheath impedance, defined by

$$i\omega C_s = 1/Z_c = \mathrm{Im}(1/Z_s). \quad (32)$$

Because the conduction and displacement currents flow in parallel, $Z_s$ may be considered the parallel combination of two impedances, $V_{s1}/J_{c1}$ and $V_{s1}/J_{d1}$. Based on the theory of linear circuits, one would expect $V_{s1}/J_{c1}$ to have the phase of an ideal resistor, 0°, and $V_{s1}/J_{d1}$ to have the phase of an ideal capacitor, −90°. Under these conditions, Eq. (32) simply yields $Z_c = V_{s1}/J_{d1}$, so that the capacitance arises solely and wholly from the displacement current.

The model, however, does not predict phases of 0° and −90° for $V_{s1}/J_{c1}$ and $V_{s1}/J_{d1}$. For example, in Fig. 2, the phase of $V_{s1}/J_{c1}$ is 10.8°, and the phase of $V_{s1}/J_{d1}$ is −87.7°. These surprising results are explained by nonlinear circuit theory [15]. A purely resistive device, if it is nonlinear, may have components of current and voltage that are out of phase, and a purely capacitive device, if it is nonlinear, may have components of current and voltage that are in phase. These unusual phase relations imply a reactive power in the resistor, and a real power in the capacitor, but these powers vanish when summed over all harmonics. When all harmonics are considered, it can be shown that a nonlinear resistor does not store any energy, and a nonlinear capacitor does not dissipate any energy.

Previous models of rf sheaths typically neglect conduction currents and assume that either the sheath voltage or current is sinusoidal. Under those conditions, symmetry forces the expected −90° phase difference between $V_{s1}$ and $J_{d1}$. Here, however, the series resistance $R$ upsets the symmetry. As $R/Z_D$ increases in Fig. 3, the phase of $V_{s1}/J_{d1}$ shifts away from the expected value of −90° (from −89.0° to −87.7°). Also, $V_{s1}/J_{c1}$ shifts away from 0° (from 4.4° to 10.8°) and the phase of $Z_s$ becomes more resistive, shifting from −87.5° to −86.4°.

Although these phase shifts are interesting, they are rather small over the range of experimental conditions studied here. As seen in Fig. 6, predicted and measured phases of $Z_s$ were always within a few degrees of −90°. (Predicted and measured phases for the total impedance are also shown; they were also in rather good agreement.) The $Z_s$ phases were so close to −90° that the capacitive sheath impedance $Z_c$ defined by Eq. (32) was within 2% of the magnitude of the sheath impedance, $|Z_s|$. Thus, within 2%, all the results reported for $Z_c$ below apply to $|Z_s|$ as well.

## V. IMPEDANCE

First, the dependence of the sheath impedance on the model input parameters will be discussed. Then the impedances predicted by the model will be compared to previous models and to experiment.

### A. Dependence on voltage

Figure 7 shows the relations between several parameters that describe the sheath width and voltage wave forms. The normalized fundamental component of the sheath voltage, $V_{s1}/T_e$, appears on the $x$ axis. As $V_{s1}/T_e$ increases, increases are seen in the other voltage amplitudes, in $W_{\max}/\lambda_D$, and in the time-averaged sheath width $W_0/\lambda_D$. The magnitude of the sheath impedance, $|Z_s|$, and the capacitive impedance $Z_c$ also increase. Plots of $|Z_s|/Z_D$ and $Z_c/Z_D$ are visually indistinguishable from the $W_0/\lambda_D$ curve.

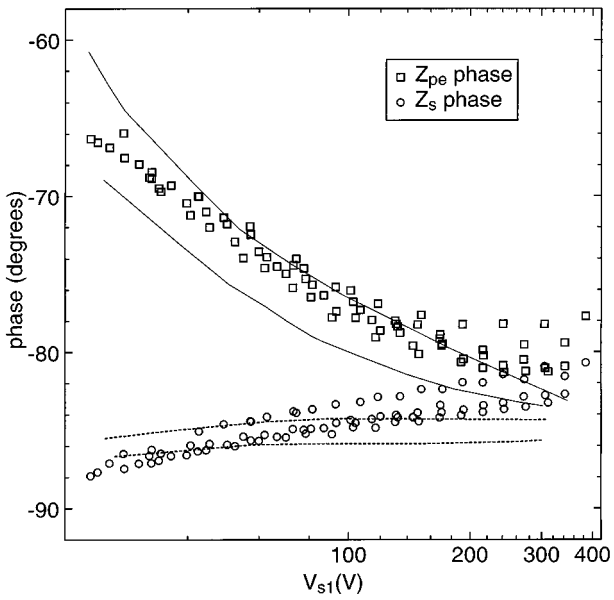


FIG. 6. Phase of the sheath impedance $Z_s$ and the total impedance $Z_{\mathrm{pe}}$ measured in a previous study [8] of argon discharges at 4.0–133.3 Pa, plotted against the fundamental amplitude of the sheath voltage $V_{s1}$. Model results, calculated for values of the input parameters corresponding to the experimental conditions, as described in Table II, are also shown. Model values of the phase of $Z_s$ fall within the range defined by the two dotted curves. Model values of the phase of $Z_a$, which corresponds to the experimental impedance $Z_{\mathrm{pe}}$ fall within the range defined by the two solid curves.

In contrast, $W_{\min}/\lambda_D$ decreases with voltage. At higher voltages, $W(t)$ becomes more sharply peaked in the vicinity of the electrode, and, therefore, the electron conduction current has less time to flow. Each pulse of electron current becomes narrower, and thus the peak value of the pulse must increase, to allow the narrower pulse to still exactly balance the ion current. Therefore the instantaneous sheath edge must approach closer to the electrode, and $W_{\min}/\lambda_D$ must decrease. Eventually, a point is reached where the sheath edge grazes the edge of the electrode. Beyond this point it is impossible to find a solution with $\langle J\rangle = 0$; only solutions with $\langle J\rangle < 0$ can be obtained. This failure indicates a breakdown in the assumptions of the model at high voltages, perhaps because harmonics in the applied voltage wave form (which is here assumed to be sinusoidal) become too large to be ignored.

As $V_{s1}/T_e \to 0$ in Fig. 7, $W_{\max}$, $W_0$, and $W_{\min}$ converge to a value

$$W_{\max}/\lambda_D = W_0/\lambda_D = W_{\min}/\lambda_D = Z_c/Z_D = 2.67. \quad (33)$$

For values of $W_{\max}/\lambda_D$ smaller than this dc limit, only solutions with $\langle J\rangle > 0$ can be obtained. Over the parameter space given in Table II, the value of this dc limit varies from 2.6 to 2.9. In the dc limit, however, the step drop in electron concentration assumed in Eq. (1) is undoubtedly a poor approximation.

Intermediate voltages in Fig. 7, in the range $8 \leqslant V_{s1}/T_e \leqslant 134$, correspond to the experimental voltage range given in Table II. In this range, $W_{\max}/\lambda_D$, $W_0/\lambda_D$, $|Z_s|/Z_D$, and

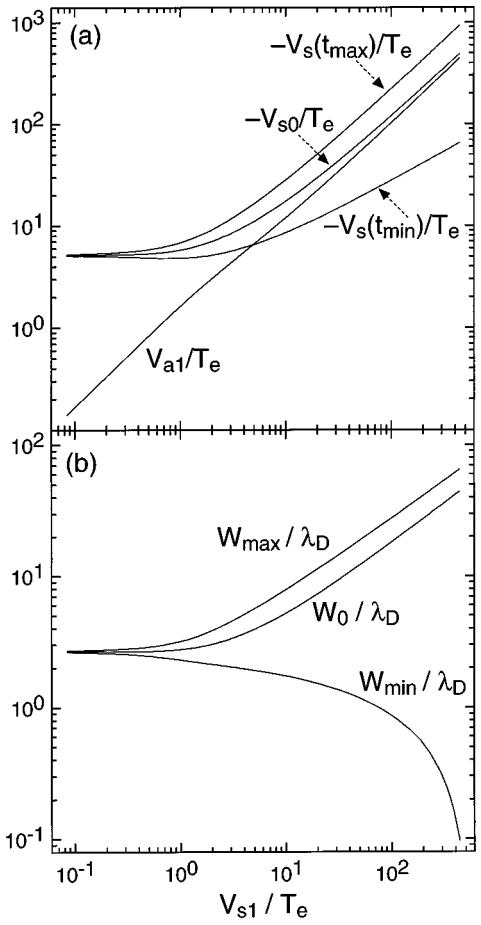


FIG. 7. (a) Relation between $V_{s1}/T_e$, the fundamental amplitude of the sheath voltage wave form, its dc amplitude $V_{s0}/T_e$, its most negative value, $V_s(t_{\max})$, and its least negative value, $V_s(t_{\min})$. The fundamental amplitude of the applied voltage, $V_{a1}/T_e$, is also shown. (b) Relation between $V_{s1}/T_e$ and the maximum, minimum, and time-averaged sheath widths $W_{\max}/\lambda_D$, $W_{\min}/\lambda_D$, and $W_0/\lambda_D$. Plots of the sheath impedance $Z_s/Z_D$ and the capacitive impedance $Z_c/Z_D$ fall on the $W_0/\lambda_D$ curve. The results were obtained by varying $W_{\max}/\lambda_D$ from 2.70 to 65. Values of the other input parameters are given in Fig. 2.

$Z_c/Z_D$ are approximately described by a power law, i.e., a straight line on the log-log plot. The slope of the log-log plot determines the power-law exponent. For $Z_c/Z_D$, the slope is given in Table III.

### B. Ion injection velocity

If the parameter $u_0/u_B$ is reduced, and all other parameters are held constant, then the ion density throughout the sheath will be reduced, as shown in Fig. 8(a). At fixed sheath width (and impedance), a lower ion density produces a lower sheath voltage. At fixed sheath voltage, a lower ion density produces a higher sheath width and impedance. These effects are illustrated in Fig. 8(b). The change in $u_0/u_B$ shifts the curve vertically without changing its shape, suggesting that the dependence of $Z_c/Z_D$ on $u_0/u_B$ is nearly an exact power law. A calculated value for the exponent of the power law is given in Table III.

TABLE III. Log-log sensitivities of $Z_c/Z_D$, the normalized capacitive sheath impedance, with respect to the dimensionless input parameters, labeled $\zeta$, and log-log sensitivities of the capacitive sheath impedance $Z_c$ with respect to the set of experimental parameters, labeled $\xi$. Sensitivities labeled ''exact'' were calculated numerically, at $V_{s1}/T_e=280$, $u_0/u_B=0.62$, $\lambda_i/\lambda_D=1.0$, $E_0\lambda_D/T_e=1.0$, $R/Z_D=3.0$, $\omega_i/\omega=0.10$, $\omega_e/\omega=27.0$, $Y_i=Y_e=0$, and $Z_c/Z_D=33.4$. Sensitivities were also obtained from the power-law exponents in Eq. (34), an approximate expression for $Z_c/Z_D$ based on the analytical solution of Ref. [2].

| | $\partial \ln(Z_c/Z_D)/\partial \ln\zeta$ | | | $\partial \ln Z_c/\partial \ln\xi$ | |
|---|---|---|---|---|---|
| $\zeta$ | Exact | Eq. (34) | $\xi$ | Exact | Eq. (34) |
| $V_{s1}/T_e$ | +0.603 | +0.600 | $V_{s1}$ | +0.603 | +0.600 |
| $u_0/u_B$ | −0.426 | −0.400 | $n_0$ | −0.426 | −0.400 |
| $\lambda_i/\lambda_D$ | +0.207 | +0.200 | $n_0$ | −0.426 | −0.400 |
| $E_0\lambda_D/T_e$ | +0.031 | 0.000 | $\lambda_i$ | +0.207 | +0.200 |
| $R/Z_D$ | −0.030 | 0.000 | $m_i$ | −0.209 | −0.200 |
| $\omega_i/\omega$ | −0.008 | 0.000 | $E_0$ | +0.031 | 0.000 |
| $\omega_e/\omega$ | +0.006 | 0.000 | $R$ | −0.030 | 0.000 |
| | | | $T_e$ | +0.006 | 0.000 |

### C. Ion mean free path

An increase in the ion mean free path $\lambda_i$ is equivalent to an increase in the ion mobility and a decrease in the Ohmic impedance associated with ion motion. But, at the high frequencies studied in this paper, this impedance is negligible. Instead, an increase in $\lambda_i$ acts to increase the sheath impedance. At higher values of $\lambda_i$, collisions are less frequent, the ions are accelerated more rapidly, and therefore the ion density profile falls farther and faster (see Fig. 8). This produces an increase in the sheath width and in its capacitive impedance $Z_c/Z_D$. The dependence of $Z_c/Z_D$ on $\lambda_i/\lambda_D$, like $u_0/u_B$, conforms closely to a power-law dependence, with the exponent given in Table III.

### D. Other model parameters

Variations in $E_0\lambda_D/T_e$, $R/Z_D$, $\omega_i/\omega$, and $\omega_e/\omega$ do not much change the overall ion density throughout the sheath. Consequently, the capacitive impedance of the sheath is rather insensitive to changes in these parameters. The log-log sensitivities to these parameters, listed in Table III, are weak. Examination of Eqs. (8), (22), and (23) show that the log-log sensitivities of $Z_c/Z_D$ to $(1+Y_i)$ and $(1-Y_e)$ are identical to those of $\omega_i/\omega$ and $\omega_e/\omega$, so the effects of secondary electrons are also quite weak.

To compare model results to experiments, it is helpful to change from the dimensionless input parameters to a new set of parameters, $V_{s1}$, $n_0$, $u_0$, $\lambda_i$, $m_i$, $E_0$, $R$, and $T_e$. Using the chain rule for derivatives, the log-log sensitivities of the impedance $Z_c$ on the new parameters can be obtained from those already calculated. Results are shown in Table III.

### E. Comparison with previous models

Although the Lieberman model of collisional sheaths [2] assumes that $u_0=u_B$, one can easily extend it to include arbitrary values of $u_0$, and obtain

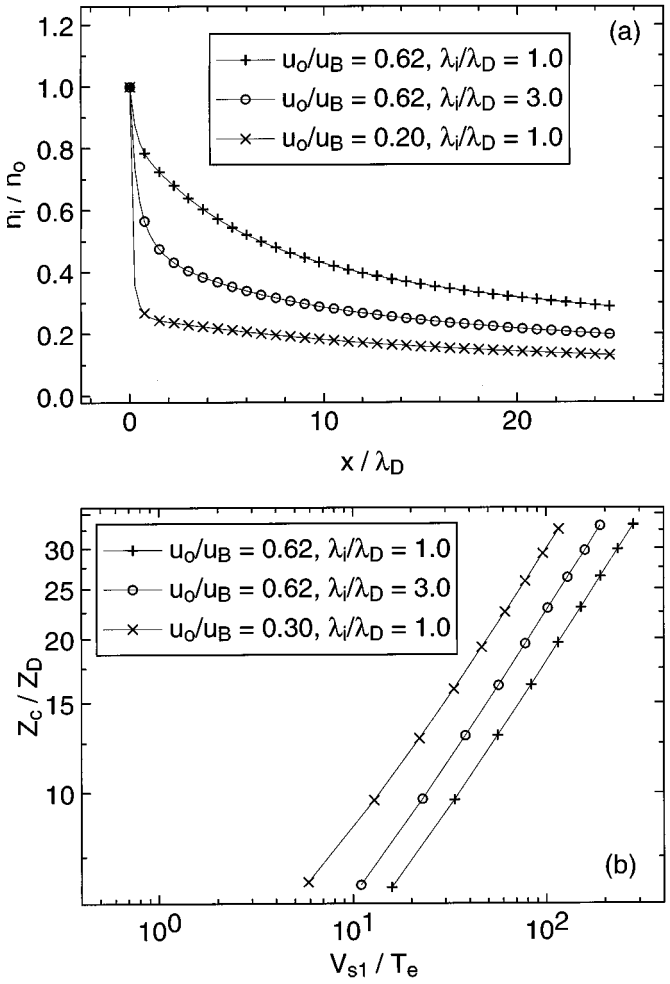


FIG. 8. (a) Ion density profiles calculated for varying values of $u_0/u_B$ and $\lambda_i/\lambda_D$, for a sheath width $W_{\max}/\lambda_D$ of 25. (b) Normalized values of the sheath capacitive impedance $Z_c$ as a function of $V_{s1}/T_e$, the fundamental amplitude of the sheath voltage, for varying values of $u_0/u_B$ and $\lambda_i/\lambda_D$, and $10 \leqslant W_{\max}/\lambda_D \leqslant 50$. Values of the other input parameters are given in Fig. 2.

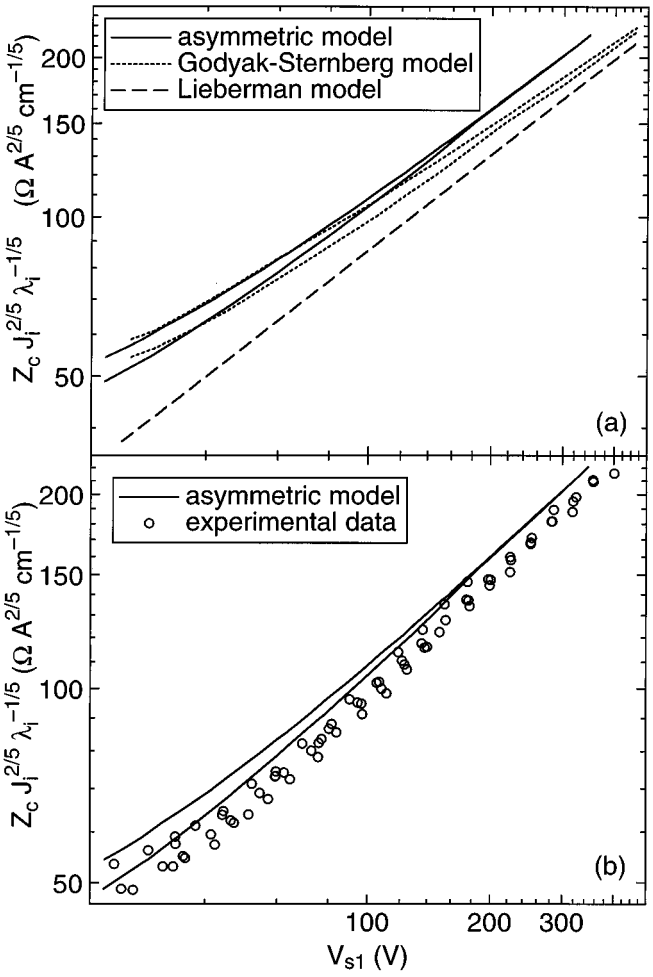


FIG. 9. Log-log plots of $Z_c J_i^{2/5} \lambda_i^{-1/5}$ vs sheath voltage $V_{s1}$, where $Z_c J_i^{2/5} \lambda_i^{-1/5}$ is a normalization of the capacitive sheath impedance $Z_c$ chosen so that predictions of the Lieberman model [Eq. (34)] fall on a single line. (a) shows values from the Lieberman model, the Godyak-Sternberg model [3], and the asymmetric discharge model presented in this paper. (b) compares the asymmetric model with experimental data from a previous study [8] of argon discharges at 4.0–133.3 Pa. At each data point, model input parameters corresponding to the experimental conditions were calculated, as described in Table II, and used in the model calculations. Results from the asymmetric model fall within the range defined by the two solid curves. Godyak-Sternberg results, calculated in Ref. [8], fall within the two dotted curves.

$$Z_c/Z_D = 0.80(V_{s1}/T_e)^{3/5}(u_0/u_B)^{-2/5}(\lambda_i/\lambda_D)^{1/5}$$
$$= 0.80(q/\omega^5 \varepsilon_0^3 A^3 m_i)^{1/5} V_{s1}^{3/5} \lambda_i^{1/5} J_i^{-2/5}. \quad (34)$$

Similarly, the collisionless Lieberman model [1] may be expressed as

$$Z_c/Z_D = 0.76(V_{s1}/T_e)^{3/4}(u_0/u_B)^{-1/2}. \quad (35)$$

The exponents from the collisional model, Eq. (34), are quite close to the log-log sensitivity factors given in Table III. [Results from Eq. (35) are not, since it is only valid at lower pressures and higher values of $\lambda_i/\lambda_D$ than are treated here.] Admittedly, the log-log sensitivity factors in Table III were calculated at a single, high sheath voltage; they do not apply at low sheath voltages. Nevertheless, the models can be compared over the entire voltage range using the plot shown in Fig. 9(a). In this log-log plot, values of $Z_c$ are multiplied by $J_i^{2/5}\lambda_i^{-1/5}$, so that the predictions of the Lieberman model, Eq. (34), fall on a single straight line of slope 0.60. The slope predicted by the asymmetric model is similar at high voltages, but it decreases at low voltages, as in Fig. 7. This behavior results from Eq. (11), the condition that the ion and electron currents balance, which determines the minimum sheath width $W_{\min}$. The Lieberman model does not include this condition—it cannot, because it neglects the conduction current. Instead, the Lieberman model assumes that $W_{\min} = 0$, which forces $Z_c$ to approach zero as $V_{s1}$ approaches zero.

Figure 9(a) also shows predictions from the Godyak-

Sternberg mode [3]. The Godyak-Sternberg model and the asymmetric model differ because the former assumes a sinusoidal current wave form and the latter assumes sinusoidal applied voltage. Although the ion density profiles and the values of $W_{\max}/\lambda_D$ and $W_{\min}/\lambda_D$ given by the two models are very similar, the different assumptions about the wave forms produce differences in the time-averaged sheath width $W_0/\lambda_D$ and in the impedance.

### F. Comparison with experiment

Experimental and model impedances are compared in Fig. 9(b). For each data point, values of the input parameters corresponding to the experimental conditions were determined, as described in Table II, and a model calculation using these input values was attempted. For some experimental conditions, above 140 V at 4.0 Pa and above 300 V at 13.3 Pa, no solutions of the model could be obtained, for the reasons discussed in Sec. V A. Model results were obtained over the rest of the experimental range; they vary with pressure in the region defined by the two solid curves in Fig. 9. In the figure, the behavior of the data and the model are quite similar. Although the $y$-axis values predicted by the model are higher than the data, the differences are within the error bounds found by propagating estimated uncertainties of $\pm 30\%$ in the measurement of $J_i$ and $\pm 1$ eV in the measurement of the electron temperature $T_e$. Errors in $T_e$ only affect the data points at low sheath voltages. Indeed, Table III indicates that the log-log sensitivity of $Z_c$ to $T_e$ is quite small at high sheath voltages. Nevertheless, as $V_{s1}/T_e$ decreases (and the dependence of $Z_c$ on $V_{s1}$ becomes weaker) the dependence on $T_e$ grows stronger. At $V_{s1}/T_e = 3.65$, for example, $\partial \ln Z_c/\partial \ln V_{s1} = 0.31$, and $\partial \ln Z_c/\partial \ln T_e = 0.29$. In the dc limit, $V_{s1}/T_e \rightarrow 0$, the voltage derivative approaches zero, and $\partial \ln Z_c/\partial \ln T_e$ increases to $\sim 0.50$, as expected from Eqs. (33) and (18).

## VI. dc SHEATH VOLTAGE

The dc offset between the $V_s(t)$ [and $V_{PS}(t)$] wave forms in Fig. 5(b) indicates that the dc sheath voltage predicted by the model does not agree with experiment. This may partly arise from experimental errors—the techniques used in Refs. [7,8] were designed to measure the rf components of $V_{PS}(t)$, not its dc level. Nevertheless, the disagreement in dc levels may also indicate a problem with the model. In particular, the values of the electric field at the sheath-presheath interface, $E_0$, used by the model may be in error.

The dc voltage drop across the sheath is quite sensitive to $E_0$. Essentially, $E_0$ contributes a time-independent voltage drop of $-E_0 W_{\max}$ to $V_s(t)$. As can be seen from Eqs. (1)–(3), $V_s(t) \leqslant -E_0 W_{\max}$, always. In dimensionless variables,

$$V_s(t_{\min})/T_e \leqslant -(E_0\lambda_D/T_e)(W_{\max}/\lambda_D). \tag{36}$$

The two sides of this inequality are equal if $W_{\min} = 0$. The two sides are approximately equal when $W_{\max} \gg W_{\min}$, as can be verified in Fig. 7. As $E_0\lambda_D/T_e$ is varied, the most negative sheath voltage $V_s(t_{\max})$ and the dc sheath voltage $V_{s0}$ vary by nearly the same amount as $V_s(t_{\min})$. Thus changes in $E_0\lambda_D/T_e$ shift the $V_s(t)$ wave form up or down in voltage, without much altering its rf amplitude or its shape.

The limit imposed by Eq. (36) could be perhaps be superseded, and better agreement obtained, if a time-varying $E_0$ were included in the model. Alternatively, less negative $V_s(t)$ wave forms, in better agreement with experiment, would be obtained at smaller values of $E_0\lambda_D/T_e$. The values of $E_0\lambda_D/T_e$ used by the model were not measured, but obtained from a model of the presheath, Eq. (26). It may be that Eq. (26) is not a valid description of the presheath. In particular, Eq. (26) assumes a Maxwellian electron energy distribution function (EEDF). But EEDFs in argon discharges are not Maxwellian; they have a large population of low-energy, ''low-temperature'' electrons at energies $<1$ eV, due to the relative absence of loss processes for electrons at low energies [16]. The electron temperature used here, from Table I, was measured at higher energies. Although this temperature may be representative of the high-energy electrons that dominate the electron conduction current given by Eq. (7), they may not yield the appropriate electric field in Eq. (26). Presheath models that include two negative species at different temperatures show that the presheath voltage, and presumably the field as well, are more sensitive to the lower-temperature species [17,18]. Thus it is plausible that the non-Maxwellian electron energy distribution is responsible for the disagreement in dc sheath voltages, but further experimental and modeling work is needed to resolve this issue.

## VII. CONCLUSIONS

The model presented here predicts current and voltage wave forms that agree more closely than previous models with wave forms measured at the rf powered sheath of a highly asymmetric cell. This good agreement is obtained because the model incorporates electrical equations that closely describe the electrical network that surrounds the powered sheath. Predicted values for $Z_c$, the capacitive impedance of the sheath at the fundamental frequency, fall within the error bounds of measured values. Impedance phases predicted by the model also agree with experiment, because conduction currents and series resistance are included. Secondary electron currents were also included in the model, but they were found to have very small effects. The experimental and model values of the dc voltage drop across the sheath were not in agreement. To explain this disagreement, further experimental and modeling work is needed. Also, consideration of applied voltage wave forms that are not sinusoidal might extend the accuracy and range of the model. Finally, it should be noted that the model presented here does not include time-dependent ion kinetics, ionization within the sheath, or external circuits that include capacitive and inductive elements in addition to series resistance. These effects may be important in discharges that differ from those studied here, either in plasma density, frequency, pressure, or cell design. Together these additional effects present important challenges for rf sheath theory.

[1] M. A. Lieberman, IEEE Trans. Plasma Sci. **16**, 638 (1988).
[2] M. A. Lieberman, IEEE Trans. Plasma Sci. **17**, 338 (1989).
[3] V. A. Godyak and N. Sternberg, Phys. Rev. A **42**, 2299 (1990).
[4] P. A. Miller, L. A. Romero, and P. D. Pochan, Phys. Rev. Lett. **71**, 863 (1993).
[5] M. Klick, J. Appl. Phys. **79**, 3445 (1996).
[6] S. Biehler, Appl. Phys. Lett. **54**, 317 (1989).
[7] M. A. Sobolewski, IEEE Trans. Plasma Sci. **23**, 1006 (1995).
[8] M. A. Sobolewski, Appl. Phys. Lett. **70**, 1049 (1997).
[9] V. A. Godyak, R. B. Piejak, and B. M. Alexandrovich, IEEE Trans. Plasma Sci. **19**, 660 (1991).
[10] M. A. Lewis, D. A. Glocker, and J. Jorne, J. Vac. Sci. Technol. A **7**, 1019 (1989).
[11] Y. Yamauchi and R. Shimizu, Jpn. J. Appl. Phys. 2, Lett. **22**, L227 (1983).
[12] H. Bruining and J. H. De Boer, Physica (Amsterdam) **5**, 17 (1938).
[13] V. A. Godyak and N. Sternberg, IEEE Trans. Plasma Sci. **18**, 159 (1990).
[14] F. F. Chen, *Introduction to Plasma Physics and Controlled Fusion* (Plenum, New York, 1984).
[15] R. Clay, *Nonlinear Networks and Systems* (Wiley, New York, 1971).
[16] V. A. Godyak and R. B. Piejak, Phys. Rev. Lett. **65**, 996 (1990).
[17] R. W. Boswell, A. J. Lichtenberg, and D. Vender, IEEE Trans. Plasma Sci. **20**, 62 (1992).
[18] R. L. F. Boyd and J. B. Thompson, Proc. R. Soc. London, Ser. A **252**, 102 (1959).
[19] M. B. Hopkins, J. Res. Natl. Inst. Stand. Technol. **100**, 415 (1995).
[20] L. J. Overzet and M. B. Hopkins, J. Appl. Phys. **74**, 4323 (1993).
[21] J. K. Olthoff, R. J. Van Brunt, S. B. Radovanov, J. A. Rees, and R. Surowiec, J. Appl. Phys. **75**, 115 (1994).
[22] M. V. V. S. Rao, R. J. Van Brunt, and J. K. Olthoff, Phys. Rev. E **54**, 5641 (1996).